ICARUS 112, 171–186 (1994)

Microwave Signatures and Surface Properties of Ovda Regio and Surroundings, Venus

R. E. ARVIDSON, R. A. BRACKETT, M. K. SHEPARD,* N. R. IZENBERG, AND B. FEGLEY, JR.

Department of Earth and Planetary Sciences and McDonnell Center for the Space Sciences, Washington University, St. Louis, Missouri 63130
E-mail: arvidson@wunder.wustl.edu

AND

J. J. PLAUT

Jet Propulsion Laboratory, Pasadena, California 91109

Received June 16, 1994; revised September 13, 1994

Magellan observations of horizontally and vertically polarized emissivity and radar specific cross sections are jointly modeled to separate dielectric constants from textural effects for lobate plains, fractured plains, fracture belts, festoon flows, and tessera in Ovda Regio and surroundings. The model assumes surface emission and scattering dominate and that signatures are controlled by a combination of quasi-specular and diffuse-scale mechanisms. Textural parameters are found to correlate with geology whereas dielectric constants are found to depend on elevation. A gradual increase in dielectric constant from rock-like values (4 to 5) to a value of approximately 50 is evident over the interval from 6054 to 6056 km, where elevations are derived from Magellan altimetry observations. Stereo radargrammetric analyses demonstrate that a return to rock-like values occurs over approximately 0.5 km above the terrain with highest dielectric constants. The abrupt return to rock-like values occurs independently of geology and reinforces the hypothesis of elevation control on dielectric constant values. Variations in dielectric constant with elevation are modeled using an 1000-ppm concentration of a ferroelectric mineral with a Curie temperature of 707 K. The model reproduces the abrupt change at highest elevations, as the Curie temperature is reached, and the gradual change as lower elevations are encountered. To our knowledge no other model explains the trends with such simplicity.

1. INTRODUCTION

One of the first-order Venus surface characteristics in Earth-based, Pioneer-Venus, Venera Orbiter, and Magellan data is the transition from lowland areas with microwave emissivities and radar-specific cross sections typical of bedrock or tightly packed debris, to highland regions with unusually low emissivities and high specific cross sections (Pettengill *et al.* 1992). Given the significant variations in surface temperature and atmospheric pressure from lowlands to highlands (~740 to ~660 K, ~90 to ~50 bar (Seiff 1983)), a plausible hypothesis is that these unusual microwave properties are governed by local ambient conditions. Various mechanisms have been proposed, including the thermodynamic stability of pyrite (FeS_2) (Pettengill *et al.* 1988, Klose *et al.* 1992) and kinetically inhibited destruction of perovskite ($CaTiO_3$) at higher (i.e., cooler) elevations (Fegley *et al.* 1993). The existence of a ferroelectric mineral phase with a temperature-dependent dielectric constant has been postulated by Shepard *et al.* (1994) and vapor transport of metal halide and/or chalcogenide volatile phases from the hot lowlands to cool highlands has been proposed by Brackett *et al.* (1994). Textural changes have also been invoked to explain the highlands signatures; specifically, volume scattering from a matrix of igneous rocks in low loss soils has been invoked to explain Earth-based depolarized radar signatures for Alpha Regio (Tryka and Muhleman 1992). Finally, Wilt (1992) showed that a volume-scattering mechanism to explain highland low emissivities would require a series of cavities imbedded in a medium with an extraordinarily low loss coefficient of <0.001.

The purpose of this paper is to use emissivity and specific cross-section data jointly to separate and understand elevation and geologic controls on microwave signatures for central Ovda Regio, the plains to the north, and the fracture belts to the south (Figs. 1–3). Ovda Regio is the largest region of high altitude/low emissivity on the planet. Six of the ten Magellan orbits with vertically polarized send/receive (VV) radar geometry cross central Ovda

* Now at Center for Earth and Space Studies, National Air and Space Museum, Smithsonian Institution, Washington, DC 20560.

0019-1035/94 $6.00

Regio, the plains to the north, and the fracture belts to the south, as do all three mapping cycles of normal (horizontally transmitted/horizontally received, HH) radar imaging. Vertically polarized emissivity (e_V) data were acquired with the vertically transmitted/vertically received (VV) data and greatly enhance the interpretation of the horizontally polarized emissivity (e_H) data. In addition, high resolution elevation data can be extracted from radar coverage over different mapping cycles and incidence angles by stereo radargrammetric techniques. This combination makes central Ovda Regio an obvious area to focus studies of scattering, emission, and surface properties.

The paper is organized in the following way. First, the geology of the Ovda Regio is discussed based on interpretations from radar mosaic data. Emissivity data are presented and discussed in the context of correlations with elevation and geology. An emission model based on surface scattering is used to separate the effects of dielectric constant and texture. Stereo radargrammetric analyses are applied to understand geologic and elevation controls at highest elevations, where emissivity and specific cross sections return to rock-like values. Joint inversions for emissivity and radar data are then presented for a set of study sites and the paper ends with the application of a ferroelectric model to explain the changes in dielectric constant with elevation.

2. RELATIONSHIPS AMONG GEOLOGY, ELEVATION, AND EMISSIVITY

The geology of central Ovda Regio was determined from examination of Magellan radar mosaics in both compressed and full resolutions, from all mapping cycles. Figure 1 provides a regional radar view of the study area, Fig. 2 is a geologic map based on the radar signatures of surface features and inferred stratigraphic relationships, and Fig. 3 shows profiles of emissivity and elevation for a north-to-south transect across Ovda Regio. Also shown in Figs. 1 and 3 are the locations of 13 study sites that were examined in detail and used for inversions of specific cross sections and emissivities. Basic data for these sites are given in Table 1. For reference, each geologic unit mapped in Fig. 2 is briefly discussed, beginning with the youngest and finishing with the oldest, as follows:

Impact craters. Ten impact craters and associated ejecta deposits were identified in the study area. Those in the plains are relatively pristine whereas those in the tessera show signs of modification. Craters on plains exhibit extensive ejecta deposits with low specific cross sections.

Corona. Several coronae were found in the plains, fractured plains, and fracture belts around Ovda Regio. None are larger than ~200 km across. Most have some associated concentric and/or radial fractures and lava flows.

Festoon flows. This unit is superimposed on the tessera in central Ovda Regio and consists of thick lava flows that cover about 4.5×10^4 km^2. The unit has been described by previous authors (Schenk and Moore 1992, Permenter and Nusbaum 1994) as a single eruptive event, consisting of several flow units with steep flow edges. This unit is of interest because the specific cross sections and emissivities vary across the outcrops in a north-to-south direction. As shown in Figs. 1 and 3 and Table 1, the southern part of the unit is the location of site 10, the highest elevation study site and one with rock-like specific cross-section and emissivity values. Site 9 is located on the festoon flow unit to the north and is only 0.9 km lower in elevation. Yet, the specific cross sections and emissivities are typical of highland signatures. These patterns suggest that the change in microwave properties is controlled by elevation and not geology.

Lobate plains. North of Ovda Regio are lowland plains with lobate features suggestive of degraded lava flow fronts. Senske *et al.* (1994) mapped this area as reticulate plains. Several coronae are present and have associated lava flows and fractures. Volcanic domes occur in clusters throughout the area. Fractures and ridges are present as well, primarily trending in a southeast–northwest direction. Extensive crater-associated deposits cover parts of the plains. This unit can also be found in pockets within the tessera. Study sites 1, 2, 4, and 6 correspond to lobate plains of different elevations. Note that the higher elevation plains have higher specific cross sections and lower emissivities (Table I) than those of the lower elevation plains, again suggesting an elevation as opposed to geologic control on microwave properties.

Fractured plains. This unit consists of lobate plains exhibiting linear fractures with two or more dominant directions of orientation. Fractured plains are adjacent to fracture belts around Ovda Regio. Some small fractured plains areas are also present within the tessera. Study site 3 is located on fractured plains.

Fracture belt. South of Ovda Regio is a "linear ridge terrain" (Solomon *et al.* 1992) interpretable as extensive fracture belts (Senske *et al.* 1994). A similar, smaller fracture belt is observed to the north of Ovda, cutting the lobate plains. These units are collections of parallel fractures, tens of kilometers apart, forming extensive linear patterns (Senske *et al.* 1994). The southern fracture belt grades northward into the tessera. Study site 13 is located on a fracture belt.

Tessera. The tessera unit is extensive, complex, and exhibits block and trough terrain with horst and graben features and linear ridge terrains described by Solomon

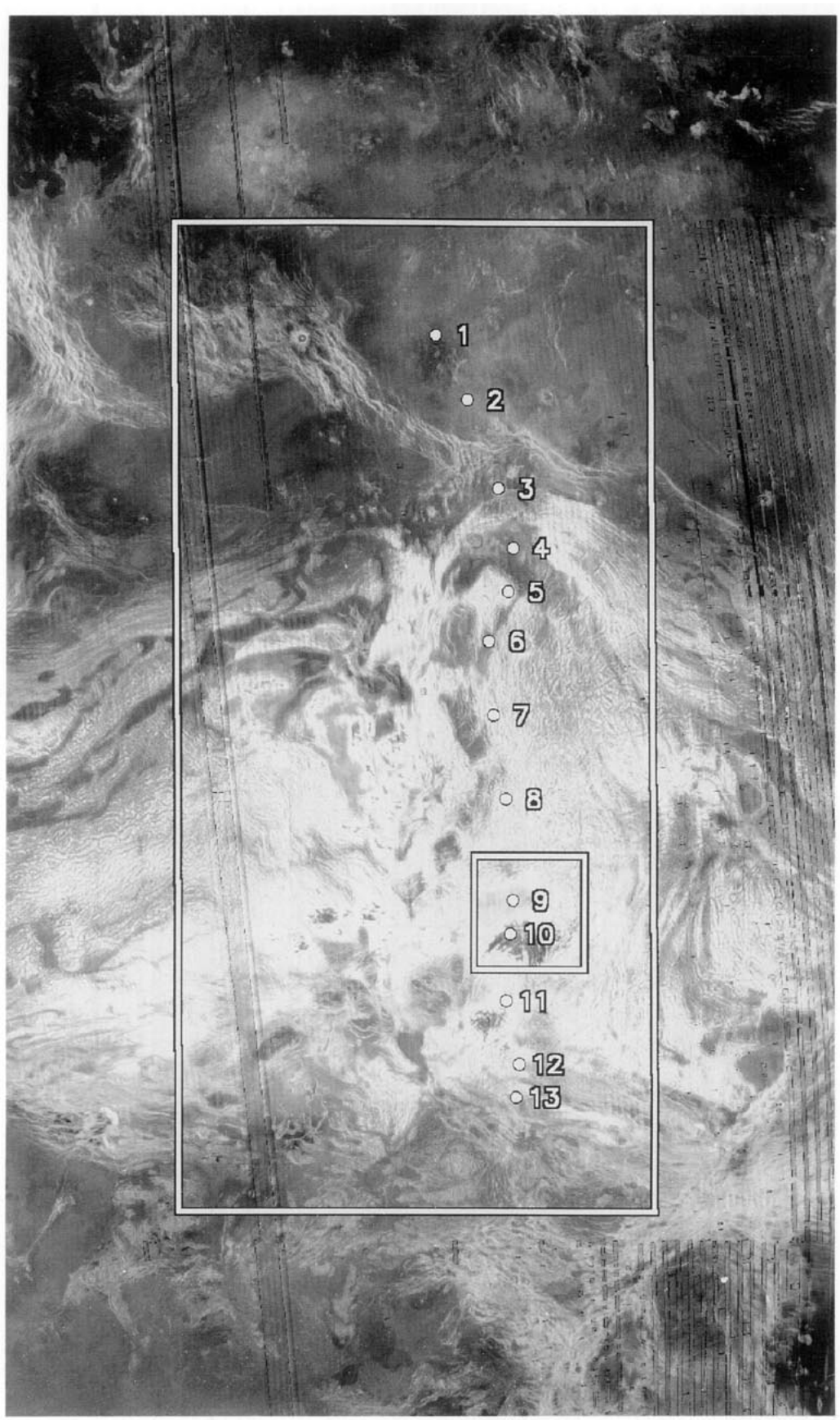

FIG. 1. Radar mosaic of Ovda Regio and surrounding plains (sinusoidal equal-area projection of the eastern portion of C2-MIDR C200N080) extending from 80°E to 108°E, 23°N to 23°S. Striping is visible where gaps in Cycle 1 image data were filled in by Cycle 2 and 3 data. The large white box (~1400 km across) outlines the region for which a geologic map is shown in Fig. 2. White dots show locations of thirteen sites where multiple angle and polarization emissivity and radar data were analyzed in detail. The festoon flow (see text for details) is located at the 9th and 10th points.

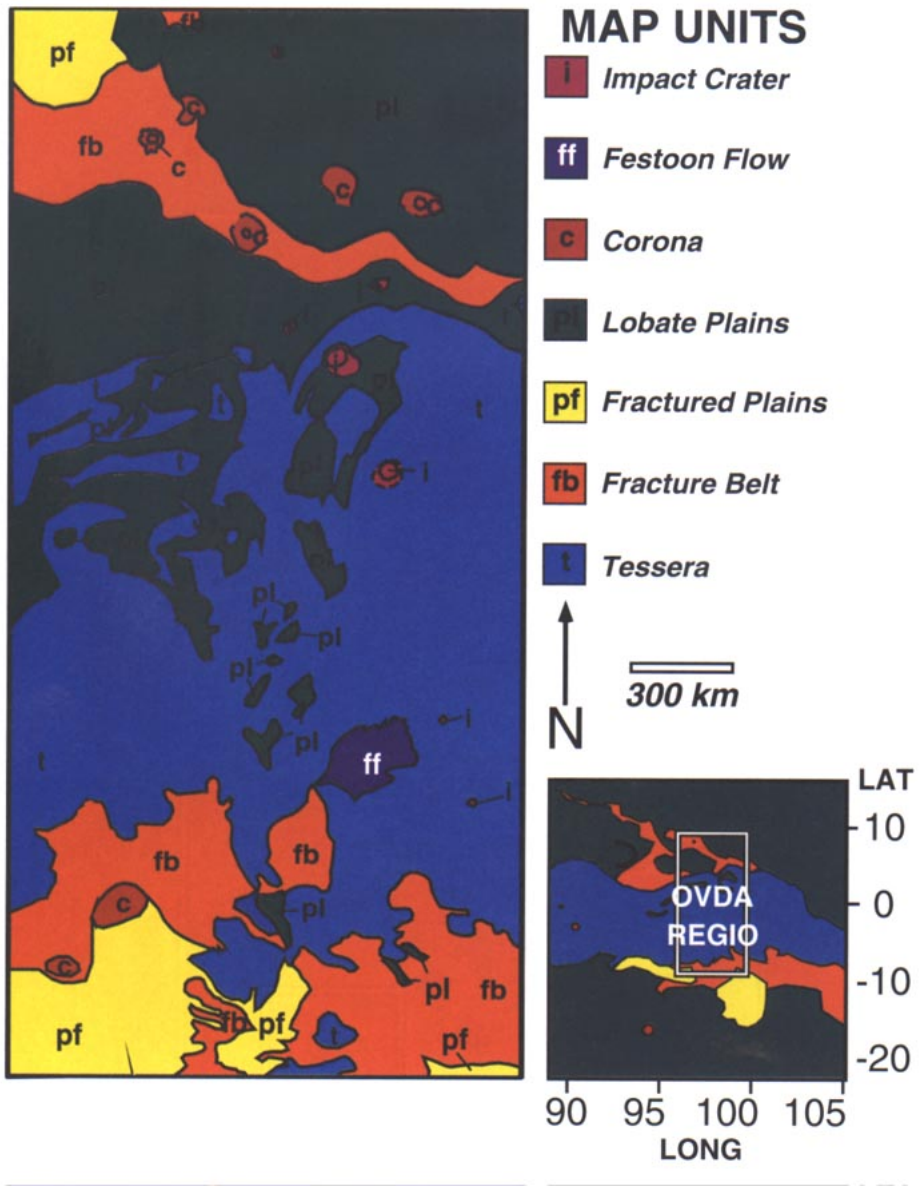

FIG. 2. Geologic map of area shown in Fig. 1, along with location map showing broad-scale geologic units. Unit descriptions: i, impact crater—craters and associated deposits; c, corona—individual volcanotectonic features; ff, festoon flows—thick lava flows covering tessera and plains units; pl, lobate plains—smooth to lightly fractured plains with degraded laval flow fronts and small (<200 km diameter) coronae and dome fields; pf, fractured plains—characterized by long (>100 km), thin (km-scale), closely spaced fractures that cross-cut in several directions; fb, fracture belts—extensive lineations with high specific cross sections interpreted as extensional features; t, tessera—combination of block and trough terrain with horst and graben features and linear ridge terrain (linear ridges with cross-cutting horst and graben features and fold-like appearances).

et al. (1992). Study sites 5, 7, 8, 11, and 12 are located on tessera. Examination of the figures and tables shows that specific cross sections increase and emissivities decrease with increasing elevation within the tessera. This trend persists even though detailed examination of radar mosaics for each tessera study site shows similar tectonic patterns and geomorphic features.

Horizontally polarized and vertically polarized emissivity data provide additional information to examine relationships among elevation, geology, and emissivity. As a first step in defining correlations, a model is employed for Fresnel emission from a flat plate by assuming that observed values of horizontally polarized emissivity e_H are given by

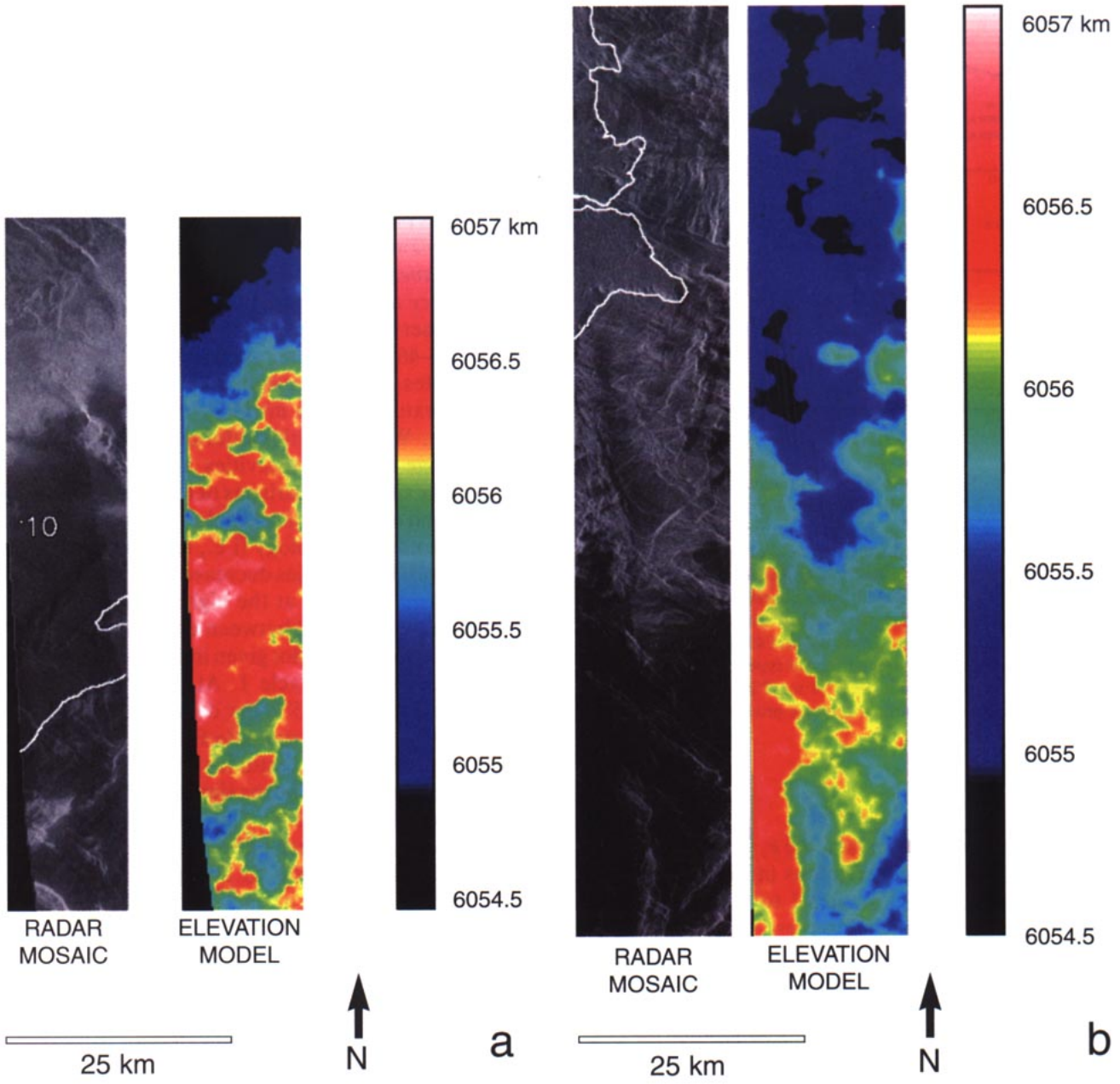

FIG. 9. (Left) Radar orthographic mosaic and elevation model for the festoon flow and surroundings. Area corresponds to the left-hand rectangle shown in Fig. 8. The flow boundary is shown as a white line. Note that the change from high to low specific cross sections does not occur at the flow boundary. Rather, low specific cross sections correspond to highest areas in the elevation model. (Right) Same as (left) but for the right-hand rectangle shown in Fig. 8. Again, low specific cross sections correlate with highest elevations and not geology.

$$e_H = 1 - \left(\frac{\cos\phi - \sqrt{\varepsilon - \sin^2\phi}}{\cos\phi + \sqrt{\varepsilon - \sin^2\phi}}\right)^2, \quad (1)$$

where ϕ is the emission angle and ε is the dielectric constant. As in previous analyses, we assume that the real component of the dielectric constant is large as compared to the imaginary component (e.g., Pettengill *et al.* 1988].

Equation (1) was solved for ε, which was used to predict vertically polarized emissivity, e_V, given by

$$e_V = 1 - \left(\frac{\varepsilon\cos\phi - \sqrt{\varepsilon - \sin^2\phi}}{\varepsilon\cos\phi + \sqrt{\varepsilon - \sin^2\phi}}\right)^2. \quad (2)$$

Equations (1) and (2) pertain only if emission is from a

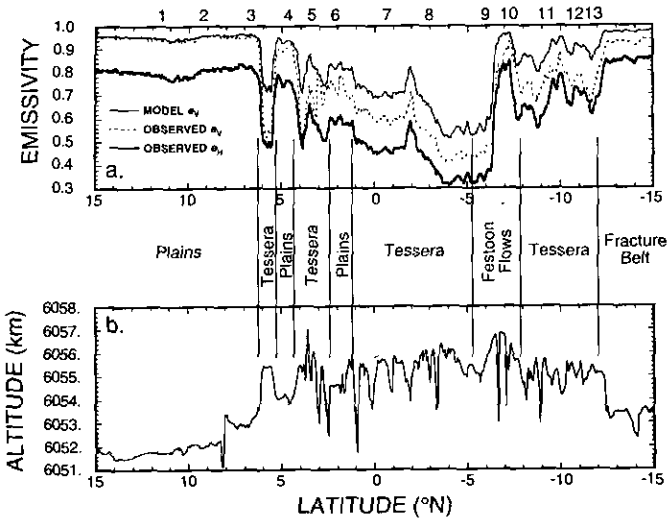

FIG. 3. (a) Plot of emissivity versus latitude (15°N to 15°S) for a region in the middle of the study site. Numbers at top correspond to the 13 study sites shown in Fig. 1. The lowermost, thick line shows values for horizontally polarized emissivity, e_H, extracted from Altimetry Radiometry Composite Data Records (ARCDR) for orbit 988. The uppermost, thin line is e_V predicted using observed e_H and assuming Fresnel emission from a flat plate. The dashed line is e_V data extracted from the ARCDR for orbit 4569. Orbits 988 and 4569 lie within 6 km of one another and usually cover similar terrain types at a given latitude. (b) Plot of radius versus latitude (−15°N to 15°N) from ARCDR for orbit 988. Terrain designations show geologic provinces along the orbit tracks.

relatively smooth surface. In fact, the e_v values calculated from Eq. (2) match the observations in the plains to the north of Ovda Regio (Fig. 3, sites 1 to 4), implying that roughness effects are small for these terrains. On the other hand, the other terrains show significant departures from the model in a direction of convergence of horizontally and vertically polarized emissivities.

To pursue more quantitatively the separation of geologic and elevation controls on emissivity, we derived a Fresnel emission model that includes quasi-specular and diffuse-scale components. The derivations are given in the Appendix. Briefly, the model includes the real component of the dielectric constant, the root-mean-square (RMS) slope (σ_{RMS}) of tilted facets with radii of curvature greater than the 12.6-cm Magellan wavelength, and two terms related to diffuse-scale processes. These latter terms include the fraction of the surface with diffuse-scale emission and an exponent related to the geometric distribution of dipoles that have diffuse-scale signatures. Figure 4a illustrates the behavior of emissivity for combinations of quasi-specular and diffuse elements and a dielectric constant of 5. Both quasi-specular roughness and diffuse emission reduce the differences between e_H and e_V. Finally, note that distinguishing between quasi-specular and diffuse effects is easiest at high emission angles. Figure 4b shows the same combination of elements for a dielectric constant of 50. Again, the effect of roughness is to cause the two emissivities to converge, as seen in the nonplains study sites.

Figure 5 illustrates the behavior of average emissivity, $\frac{1}{2}(e_H + e_V)$, for various textural parameter values. Also shown on this plot is the average emissivity for a flat plate (i.e., $\sigma_{RMS} = 0$ and no diffuse component). The significant point is that *average emissivity is approximately independent of surface texture,* up to incidence angles of 60°. The Magellan observations that we present are at incidence angles of 25°–46°. Therefore, assuming that Fresnel emission dominates, first-order separation of dielectric constant from texture can be made by averaging e_H and e_V observations. We utilize this information by plotting in Fig. 6 average model emissivities and data for the 13 detailed study sites. Comparisons of the average emissivities (Fig. 6) and elevation data (Table 1) show a correlation that is independent of geology (i.e., textural effects have been removed). Emissivities decrease with increasing elevation and then decrease at the highest elevation (study site 10). The overall trend between emissivity and elevation is summarized in the plot given in Fig. 7 using horizontally polarized data for cycle 1. At the emission angles for the observations (~45°), the data would need to be shifted to lower values to simulate Fresnel emission from flat plates, with the shift magnitudes given by the dielectric constant and roughness. The maximum emissivity correction would only be about 0.05. Thus, even with roughness effects removed, the pattern between elevation and emissivity would still be similar to that presented in Fig. 7 (i.e., a gradual decrease in emissivity between 6054 to 6056 km and then an abrupt return to normal values above the latter elevation).

3. RETURN TO NORMAL CONDITIONS AT HIGHEST ELEVATIONS

In this section we investigate the elevation and geologic controls on the change from low emissivity and high specific cross-section values to rock-like signatures at the highest elevations in the study area. Specifically we discuss height information generated from digital elevation maps derived from mapping cycle 1 and 3 radar images over the festoon flow unit using the Vexcel Magellan Stereo toolkit software (Leberl *et al.* 1992). Figure 8 shows a regional-scale radar mosaic of the festoon flows and surrounding tessera, along with the regions for which digital elevation models were generated from stereo radargrammetry. Figure 9 presents orthographic radar mosaics (i.e., corrected for relief displacement) and elevation models for the two subareas. The elevation models were tied to the altimetric data through the elevation for site 10

TABLE I
Microwave Properties of Ovda Regio Study Sites

Site number	1	2	3	4	5	6	7	8	9	10	11	12	13
Elevation (km)	6051.8	6051.9	6053.0	6053.7	6054.2	6054.4	6055.5	6055.8	6055.2	6056.1	6055.8	6055.3	6055.4
Cycle 1													
HH (db)	−15.2	−13.5	−13.3	−16.1	−8.5	−14.1	−3.8	−4.0	−6.0	−13.3	−2.8	−2.7	−4.9
e_H	0.79	0.81	0.79	0.75	0.61	0.57	0.48	0.43	0.41	0.81	0.61	0.52	0.56
Incidence (°)	45.8	45.9	45.8	45.6	45.5	45.3	44.9	44.5	43.7	43.4	42.7	42.2	41.9
Cycle 2													
HH (dB)	−9.3	−9.0	−8.7	−9.7	1.5	−8.0	2.3	1.9	−1.1	−9.9	2.2	1.4	0.9
e_H	0.87	0.9	0.88	0.87	0.6	0.65	0.56	0.46	0.42	0.89	0.63	0.59	0.59
Incidence (°)	24.8	24.8	24.8	24.8	24.8	24.8	24.8	24.8	24.8	24.8	24.8	24.8	24.8
Cycle 3													
HH (dB)	−10.4	−8.9	−9.7	−10.3	−0.5	−8.0	−1.8	−0.2	−1.2	−10.2	0.8	1.7	−1.8
e_H	0.86	0.87	0.86	0.85	0.63	0.66	0.57	0.47	0.42	0.9	0.67	0.57	0.61
Incidence (°)	25.6	25.5	25.3	25.1	25.0	24.8	24.4	24.1	23.5	23.3	22.8	22.4	22.2
Cycle 3													
VV (dB)	−15.5	−13.3	−14.3	−14.8	−5.0	−13.6	−3.2	−4.8	−6.7	−14.1	−2.8	−2.3	−6.5
e_V	0.94	0.96	0.95	0.91	0.66	0.71	0.61	0.55	0.49	0.84	0.72	0.63	0.72
Incidence (°)	45.6	45.6	45.5	45.4	45.3	45.1	44.6	44.1	43.4	43.1	42.4	41.8	41.5
VV/HH ratio[a]	0.9	1.1	0.8	1.3	2.2	1.1	1.2	0.8	0.9	0.8	1.0	1.1	0.7

Note. Each mapping cycle corresponded to a 243-day transect of the spacecraft around the planet. HH stands for horizontally polarized transmit and receive data given as specific cross section. VV stands for vertically polarized transmit and receive. e_H, e_V stand for horizontally and vertically polarized surface emissivity, respectively. Elevations are derived from Magellan altimetry using ARCDR standard products. Elevations are averaged over emissivity footprints. Sites 1–4, 6: Plains. Sites 5, 7–8, 11, 12: Tessera. Site 9: Bright festoon flow unit. Site 10: Dark festoon flow unit. Site 13: Fracture belt.

[a] Comparison of Cycle 3 VV and Cycle 1 HH

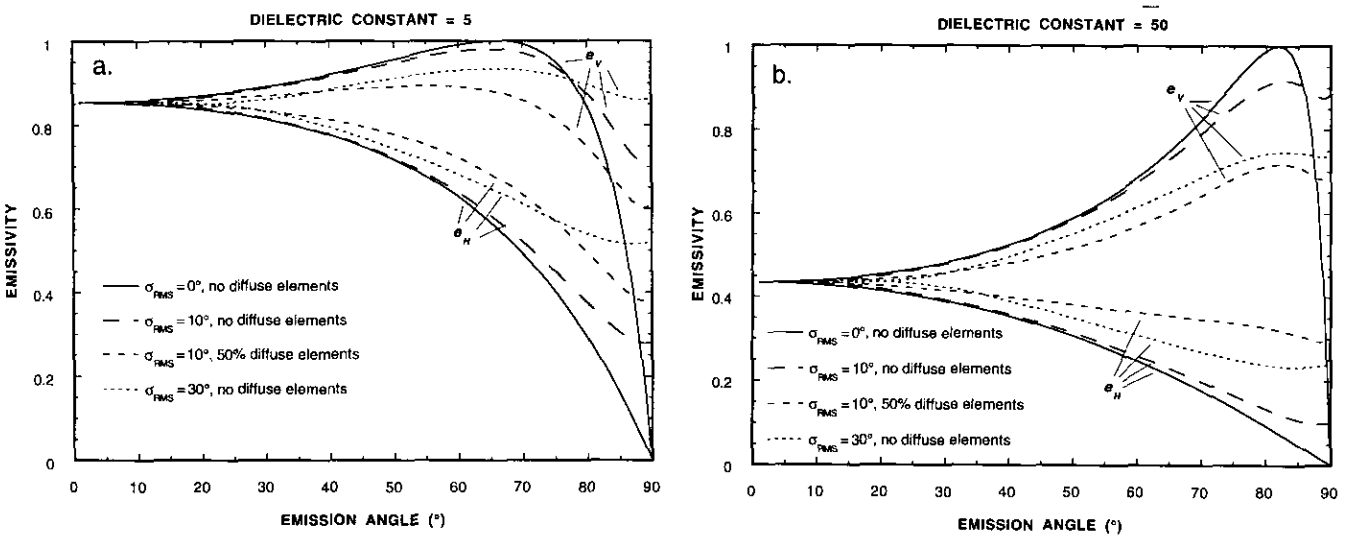

FIG. 4. (a) Plot of model Fresnel emissivity versus emission angle for combinations of RMS slope (σ_{RMS}) and fraction of emission caused by diffuse elements. The dielectric constant of the surface is 5 for all curves. The point where e_V becomes unity is the Brewster angle. Note that the greatest separation between e_H and e_V at typical emission angles of 25°–45° occurs for smooth surfaces. Increasing RMS slope and/or a fraction of diffuse scatterers causes e_H and e_V to converge. (b) Similar to (a) but with a surface dielectric constant of 50. The Brewster angle has shifted to a higher emission angle and emissivities are significantly lower than those shown in (a). Other trends are similar to those noted above.

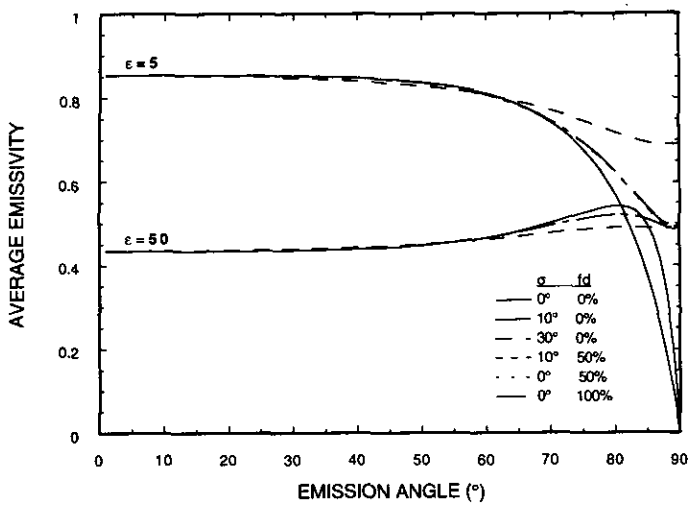

FIG. 5. Plot of average Fresnel emissivity $((e_H + e_V)/2)$ versus emission angle for models shown in Fig. 4. Note that for any value of RMS slope or fraction of diffuse scatters, the average emissivity is approximately constant for emission angles <60°. Therefore, in this range of emission angles, the average Fresnel emissivity can be used to provide an estimate of the dielectric constant, independent of surface roughness, under the assumption that Fresnel emission dominates.

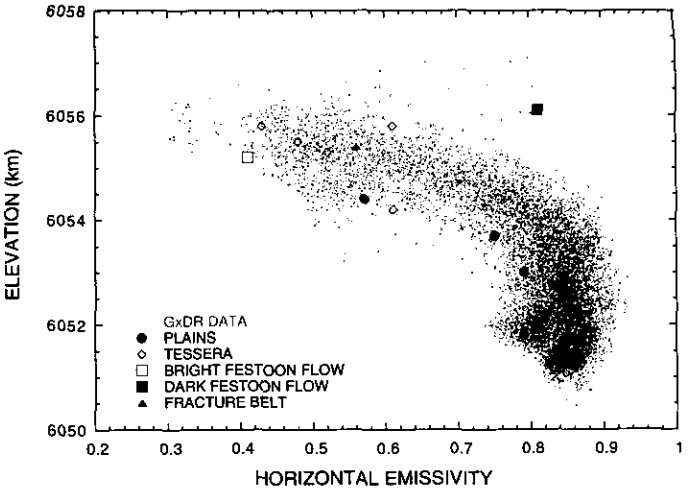

FIG. 7. Horizontally polarized emissivity plotted as a function of elevation for the area contained in the larger white box shown in Fig. 1. Data extracted from Global Data Records (GxDRs). In addition, data for the 13 study sites are grouped by geologic units and plotted as distinct symbols, using data given in Table 1 and Fig. 2. Note the gradual decrease in emissivity with increasing elevation. Values range from 0.8 to 0.9 up to 6054 km and then decrease to values as low as 0.3 between 6054 to 6056 km.

(i.e., the elevation model was shifted to have the same elevation as the altimetric data provide for site 13). Comparisons of the elevation models with individual altimetric elevation echoes show that both the altimetry and elevation models have the same broad-scale trends. The elevation data derived from stereo analyses thus provide broad trends and detailed topographic information.

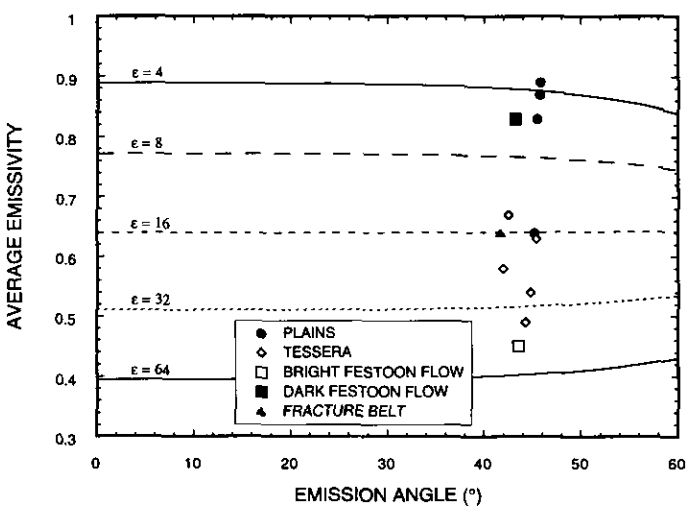

FIG. 6. Average emissivity plotted for various dielectric constants along with data for the 13 study sites. Based on results shown in Fig. 5 and discussed in the text, the average emissivity removes roughness effects (e.g., effects related to geology). The plot suggests that the dielectric constants for the study sites range over more than an order of magnitude. Also note that the inferred dielectric constants for the festoon flow vary by an order of magnitude. The lower value corresponds to the higher elevation site.

It is clear from examination of the elevation models and the radar mosaics that the change at highest elevations from high to low specific cross sections occurs independently of geology. This impression is reinforced by examination of the low specific cross-section areas on the tessera located in the eastern part of the mosaic shown in Fig. 8. Slightly raised blocks (horsts) have low specific cross sections whereas the surrounding valleys (graben) have high values. The elevation change is only a few hundred meters, based on the incidence angles of the observations and the width of the slopes in the images. The observation that the change back to rock-like values occurs over a small elevation range is further quantified in Fig. 10, a plot of elevations derived from stereo analyses versus specific cross section.

4. INVERSIONS OF EMISSIVITY AND SPECIFIC CROSS-SECTION VALUES FOR STUDY SITES

In this section we utilize the Fresnel emission model, augmented with predictions for radar backscatter, to invert for dielectric constant and roughness using emissivity and radar data (Table 1) for the 13 study sites. The backscatter component of the model is derived in the Appendix. The model predicts that HH specific cross sections are equivalent to VV specific cross sections for a given incidence angle. This is clearly a simplification, but one consistent with the data shown in Table 1.

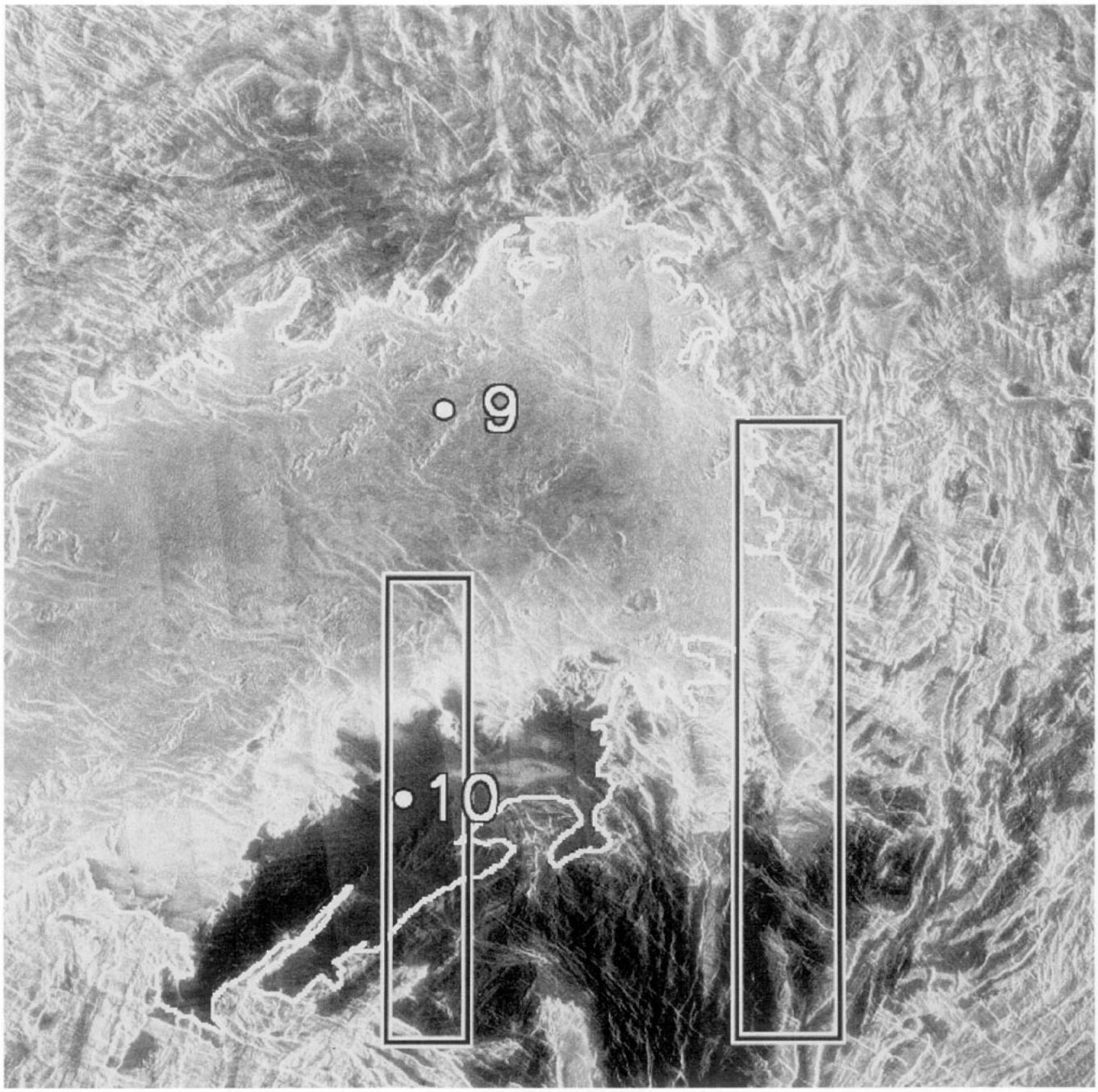

FIG. 8. Radar mosaic of the festoon flow region generated from MIDRs F05S098 and F05S093 (−3.27°N to −7.63°N, 94.52°E to 98.92°E). The mosaic covers the area shown as a small white box in Fig. 1. Rectangles show areas for which elevation data were extracted using radar stereogrammetry techniques. The smaller rectangle is ~25 km wide. White line traces boundary of festoon flow and numbers show locations of the two study sites within the flow. Note that the change from high to low specific cross sections does not occur at the flow boundaries. Also note to the right of the second rectangle the raised blocks of tessera with low specific cross sections.

For the inversions, all emissivity and horizontally polarized specific cross-section data were utilized. Vertically polarized radar data were omitted because the images appear noisy and because the values are for the most part comparable to cycle 1 HH data. Table II lists the results of the model inversions. Briefly, the inversion procedure was nonlinear and based on a grid search technique (cf. Bevington 1969). A set of forward models was calculated

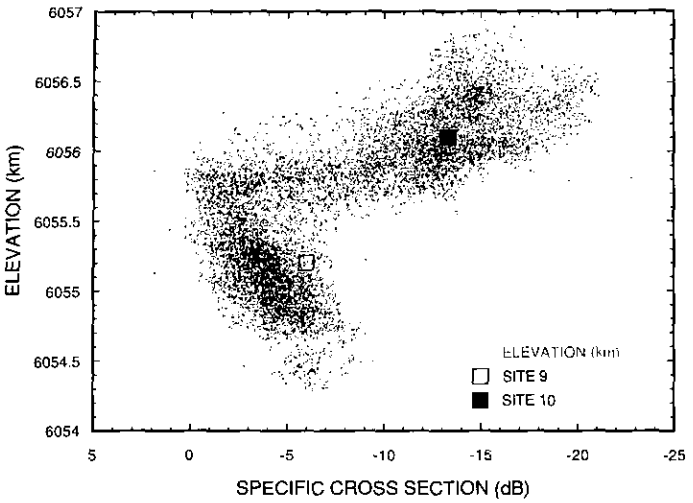

FIG. 10. Elevation model data plotted as a function of specific cross section (cycle 1 data) for both areas covered in Fig. 9. Study sites on the festoon flow are also plotted. Note that the change from high to low specific cross sections occurs over only ~0.5 km, in contrast to the 2-km range observed for the decrease in emissivity with increase in elevation shown in Fig. 4.

for a wide range of model parameters. The χ^2 difference between the observed data and each forward model was computed and the set of model parameters that minimized the χ^2 was chosen as an approximate solution. A second set of forward models was then calculated by limiting the range of model parameters to be close to the approximate solution. The procedure was followed iteratively until χ^2 values remained constant and low.

As shown in Table II, the best fits were for plains and the festoons flows: terrains that are morphologically smooth in radar images and that produce values consistent with smooth surfaces at the subpixel scale. Also, estimated dielectric constants for all terrains are close to those inferred from average emissivity of a plate. Results of the inversion are encouraging in that roughness parameters correlate directly with geology. Consider that σ_{rms}, fraction of diffuse-scale scatters, f_d, and the diffuse-scale exponent terms, n, are systematically lower for plains than those for tessera. Of most importance, the dielectric constant is predicted to increase with increasing altitude, regardless of terrain type. In sum, results suggest that elevation and geology control emissivity and specific cross section and that the two effects can be separated to first order, although more complex models are clearly needed to explain fully emission and scatter from rough terrains.

5. FERROELECTRIC MODEL OF HIGHLANDS EMISSIVITY

The presence of ferroelectric minerals phases in the venusian highlands was first proposed by Shepard *et al.* (1994), who used emissivity data (as a proxy for dielectric constant) that were not corrected for roughness effects. In this section, we expand upon this idea in two ways. First, we use dielectric constants given in Table II to determine if a ferroelectric model is reasonable for the study sites. Second, we consider forward models of how surfaces with given ferroelectric properties would appear in emissivity data, given a range of terrain types within any given emissivity footprint, the hypsometry of the Ovda Regio area, and likely errors in elevation observations.

Ferroelectric minerals have unusual dielectric properties; below a compositionally dependent temperature,

TABLE II
Results of Dual Radar and Emissivity Inversions

Site	Description	Elevation (km)	ε	σ_{RMS} (°)	f_d (%)	n	χ^2
1	Lobate plains	6051.8	4.2	10	15	1.2	0.0041
2	Plains w/ lineations and domes	6051.9	3.7	12	24	1.0	0.036
3	Slightly fractured plains	6053.0	4.3	9	20	2.0	0.015
4	Medium altitude plains	6053.7	5.2	9.5	11	1.0	0.033
5	Tessera	6054.2	13.5	17	60	1.85	2.1
6	Higher altitude plains	6054.4	12.7	5	36	1.0	0.32
7	Tessera	6055.5	28.0	13	54	1.2	2.2
8	Tessera	6055.8	37.0	11	36	2.0	1.0
9	Bright interior of festoon flow	6055.2	49.0	9	33	1.8	0.29
10	Dark interior of festoon flow	6056.1	4.45	7	31	1.25	0.13
11	Tessera	6055.8	17.5	13	66	2.0	0.97
12	Tessera	6055.3	24.5	13	42	2.0	0.94
13	Fracture belt	6055.4	24.5	13	42	1.9	3.5

Note. Elevations are derived from Magellan altimetry using ARCDR standard products and are averages over areas covered by emissivity footprints.

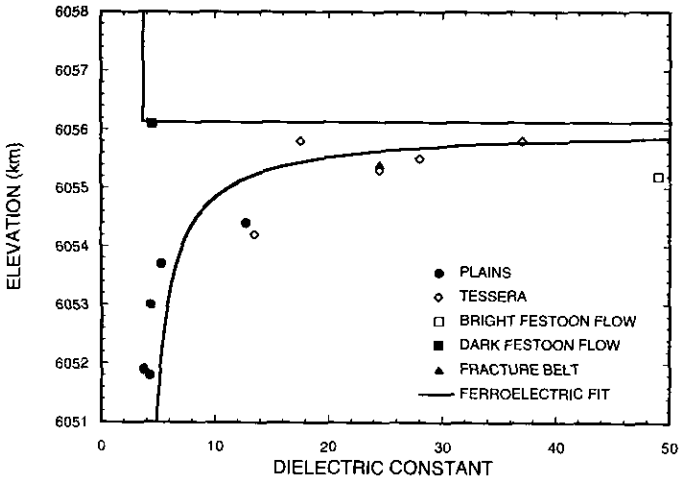

FIG. 11. Plot of dielectric constant versus elevation for the 13 study sites. Dielectric constants are inferred from dual inversions of emissivity and radar are as reported in Table II and are interpreted to be independent of roughness (i.e., geology). Also shown is a best-fit line (determined by minimizing the sum of the squares of the differences between model and observed dielectric constant) for a ferroelectric model in which the dielectric constant is modeled as a function of temperature. See text for details of model parameters.

called the Curie temperature, the dielectric constants are in the range of 10–100. However, at the Curie temperature, the dielectric constants dramatically increase, often to values as high at 10^5 (Burfoot 1967). As temperature increases above the Curie temperature, the dielectric constant follows the Curie–Weiss relationship

$$\varepsilon = \frac{C}{T - T_c} \quad \text{for } T > T_c, \tag{3}$$

where C is a constant called the Curie constant, T is temperature, and T_c is the Curie temperature. Mixing models for two-component mixtures of dielectrics indicate that as little as 0.1% by volume of a ferroelectric mineral phase is required to explain the lowest emissivities observed on Venus using Fresnel emission from a plate (Shepard *et al.* 1994). Shepard *et al.* (1994) also showed that the behavior of Eq. (3) closely replicates the average emissivity behavior with elevation on Ovda Regio. Furthermore, the behavior of ferroelectrics predict the observed abrupt return to more normal dielectric constants and emissivities above the Curie temperature.

Figure 11 is a plot of elevation versus dielectric constant for the 13 study sites. Also shown is the best-fit ferroelectric model. The model parameters were determined by minimizing the sum of the squares of deviations between observed and model dielectric constants. The data are reasonably well fit by the model, given the range of terrain types and the simplicity of the model used to separate dielectric constant from roughness. The solution shown in Fig. 11 requires that the ferroelectric phase be present at a (volume) abundance of 1000 ppm and with a Curie temperature of 707 K.

Monte Carlo forward models of elevation-dependent emissivity were also performed to evaluate the variance in the observed emissivity and elevation data and the extent to which the data are explained by a ferroelectric model. Figure 12 shows three examples of Monte Carlo simulations (12a–12c), as well as the observed emissivity and elevation data over Ovda Regio (12d). Each figure is a plot of emissivity versus altitude. In Fig. 12a, 10,000 points were given random elevations between 6050 and 6058 km. The dielectric constant of each point was determined using the temperature vs elevation relationship of Eq. (3) and the parameters obtained for the study site fit. In addition, each point was viewed at a randomly determined emission angle between 38° and 46° (appropriate for Magellan observations of Ovda Regio). The horizontal emissivity was then calculated using a flat plate (Fresnel) model with the determined dielectric constant and emission angle for each point. In Fig. 12b, 10,000 elevations were randomly determined, constrained by the hypsometric distribution for Ovda Regio (as determined from the altimetry data covering the latitudes 23°S to 23°N and longitudes 80°E to 108°E). The dielectric constant and emission angle of each point were determined as in Fig. 12a. Additionally, each point was given a random normally distributed (with a standard deviation of 2°) slope. Finally, each point was given a random fraction of diffuse scattering (between 0 and 50%) to simulate textural effects. The horizontal emissivity of the nondiffuse fraction was determined using a flat plate model. The emissivity of the diffuse fraction was assumed to be equivalent to the average of the horizontal and vertical emissivity. Figure 12c was determined using the same parameters as Fig. 12b but with three additional effects. First, errors in Magellan altimetry were simulated by adding a random normally distributed noise component (with a standard deviation of 100 m) to the altitude. Additionally, rather than using a single critical temperature for the ferroelectric model, a range of critical temperatures, normally distributed with a standard deviation of 2°C, was used. Finally, each point was assumed not to lie at a single elevation, but to consist of 10,000 subpixels with a range of elevations normally distributed with a standard deviation of 100 m.

Figure 12d shows the actual emissivity and altimetry data over Ovda Regio (extracted from the area covering the latitudes 23°S to 23°N and longitudes 80°E to 108°E). The small points are altimetry data. The larger circles are derived from stereo data for the two areas shown in Fig. 9. The solid line is the ferroelectric model fit used in the Monte Carlo simulations of Fig. 12a–12c. Agreement between the observed data of Fig. 12d and model data of

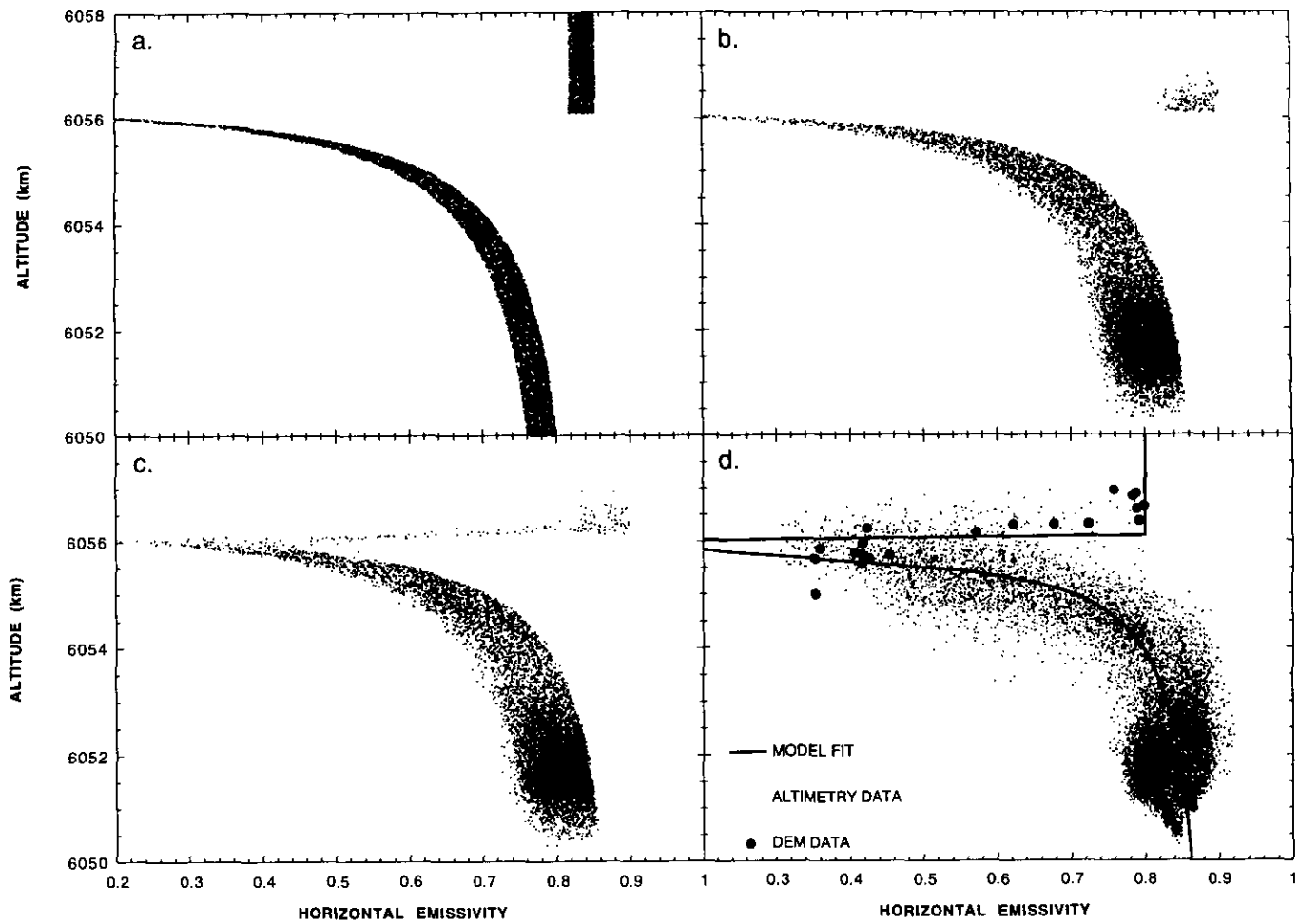

FIG. 12. Plot of emissivity (e_H) versus emission angle for Monte Carlo simulations (a–c) and the observed emissivity and elevation data over Ovda Regio (d). (a) Monte Carlo simulation of emissivity versus emission angle predicted by the ferroelectric model including the effects of variable emission angle and elevation. (b) Monte Carlo simulation of emissivity versus emission angle predicted by the ferroelectric model including the effects of variable emission angle, elevation (constrained by the hypsometry of Ovda Regio), surface slope, and diffuse emission. (c) Monte Carlo simulation of emissivity versus emission angle predicted by the ferroelectric model including all of the effects of (b) and: (1) Errors in Magellan altimetry simulated by adding a random normally distributed noise component (with a standard deviation of 100 m) to the altitude. (2) Use of a range of ferroelectric critical temperatures. A normally distributed variation with a standard deviation of 2 K was used. (3) Modeling a range of elevations assuming a normally distributed variation with a standard deviation of 100 m. (d) The actual emissivity and altimetry data over Ovda Regio (extracted from the area covering the latitudes 23°S to 23°N and longitudes 80°E to 108°E). The small points are altimetry data. The larger circles are elevation data from stereo radarphotogrammetry. The solid line is the ferroelectric model fit used in the Monte Carlo simulations of (a–c), assuming a 43° emission angle.

Fig. 12c is compelling. The major difference between the two plots is the wider spread about the ferroelectric curve fit observed in the actual data. In reality, altimetry in highland regions has large errors due to multiple echoes whereas altimetry from smooth lowland plains has small errors. Thus, modeling altimetry error with a single standard deviation is simplistic; however, it is unjustified to include more complicated (e.g., elevation dependent) altimetry errors. It is clear that the ferroelectric model is consistent with the observed distribution of emissivity versus elevation, after the expected variance is included.

The primary difficulty with the ferroelectric model is the geochemical feasibility of ferroelectric phases existing on Venus. We therefore briefly review two possibilities based on venusian geochemistry and terrestrial analogs.

(a) The minerals are ubiquitous on the surface and produced by volcanism. For example, consider the mineral perovskite, which is actually a series of phases with the structure ABX_3, where the X is typically oxygen (Deer *et al.* 1963). The most common perovskite, $CaTiO_3$, is not ferroelectric. However, substitution of Ba, Sr, Cd, or Pb for Ca produces a suite of solid–solution ferroelectrics (Rupprecht and Bell 1964, Kingery *et al.* 1976). Likewise,

the substitution of Sn, Hf, Zr, Ce, Ta, Nb, and Cr for Ti also produces ferroelectric behavior (Kingery *et al.* 1976, Lines and Glass 1977). Knopite is a perovskite containing 2–3% Ce, La, and Y oxides and has been reported in alkaline basalts from Uganda and syenites in the Aln region of Sweden. Niobian perovskite from the Kaiserstuhl in Germany contains up to 26% Nb_2O_5 (Deer *et al.* 1963). Although much of the chemical analysis of the venusian surface indicates the presence of tholeiitic basalt, at least two landers (Venera Landers 8 and 13) measured compositions compatible with alkaline rocks. Fegley *et al.* (1993) also noted that alkaline rocks can buffer the atmospheric concentrations of CO_2, HCl, and HF. Furthermore, Kargel *et al.* (1991, 1994) have observed that some of the venusian channels require low viscosity melts and suggested carbonatite flows as one possibility. Also, as noted by Shepard *et al.* (1994) pyrochlore minerals are also found in alkaline volcanic rocks and can exhibit ferroelectric properties.

(b) The ferroelectric phases are surficial deposits produced by volcanic exhalations that deposit selected ferroelectric phases widely or perhaps preferentially on (cool) highlands. Large enrichments of volatile metals (e.g., Cu, Zn, Sn, Pb, As, Sb, Bi) are observed in terrestrial volcanic aerosols, and by analogy, metal halides and chalcogenides are likely to be the product of venusian volcanism (Brackett *et al.* 1994). The combination of the high vapor pressure of metal halides and chalcogenides at Venus surface temperatures and the venusian vertical temperature gradient can transport these phases to the highlands of Venus where condensation will occur. Many metal halides and chalcogenides have high dielectric constants (Young and Frederikse 1973) and many are also ferroelectric. Specifically, the following minerals exhibit ferroelectric properties: WO_3, SbSI, GeTe, $CsGeCl_3$ (Lines and Glass 1977), antimonite (Mozgova *et al.* 1977), stibiotantalite (Gavrilova *et al.* 1970), $Gd_2(MoO_4)_3$ (Yesayan *et al.* 1974), $CuSbS_2$ (Grigas *et al.* 1976), chalcocite (Cu_2S), and perhaps djurleite (Bieniulis *et al.* 1987). Corry (1984) states that 15 ore or related minerals are known ferroelectrics, 56 minerals are isostructural with these 15 ferroelectrics, and another 60 ore minerals may be ferroelectric.

6. CONCLUSIONS AND IMPLICATIONS

In this paper we have separated dielectric constant and roughness values for regions in and around Ovda Region using horizontally and vertically polarized emissivities, radar backscatter, and a straightforward modeling approach. Dielectric constants were found to be directly related to elevation, whereas roughness values were found to be controlled by geology (i.e., terrain type).

The gradual decrease in dielectric constant with increasing elevation and the abrupt transition to more rock-like values at the highest elevations was modeled using a small concentration of a ferroelectric mineral. The ferroelectric hypothesis satisfies all the observations with a minimum of assumptions. The ferroelectric mineral candidate(s) may be phases in volcanic rocks or, more likely, volatile metal phases that are the result of volcanic emissions, perhaps preferentially transported to the highlands.

Further work needs to be conducted to explore the ferroelectric hypothesis, including examination of Magellan data over other highland areas and more detailed consideration of geochemical plausibility. Ultimately, a highland lander would be needed to test the ferroelectric hypothesis, together with other hypotheses that have been postulated to explain highland microwave signatures. An imaging system would provide information on the extent to which the surface has been weathered or if there are spherical cavities in outcrops. Imaging could also be used to search for other evidence indicative of unusual mineralogy, such as metallic luster suggestive of plating on outcrops. X-ray diffraction could be used to identify mineralogy of selected soil samples, followed by X-ray fluorescence for elemental abundance (Vaniman *et al.* 1991, Klingelhöfer *et al.* 1992]. These geochemical measurements may not have the sensitivity needed to identify trace constituents causing ferroelectric signatures. Thus, perhaps the best test would be to measure for selected samples the dielectric constant at different temperatures.

APPENDIX: DERIVATIVE OF THE MICROWAVE SCATTERING MODEL

Introduction

We treat the microwave signature of a surface observed in either reflection or emission as being due to a combination of quasi-specular and diffuse-scale emission or scattering from the surface (i.e., volume emission and scattering is ignored). The Kirchhoff approximation (i.e., a geometric optics formulation) is used to model quasi-specular emission and scattering (Ulaby *et al.* 1982) and an empirically derived formulation is used to model diffuse-scale phenomena (Hagfors and Evans 1968, Pettengill *et al.* 1988). In this Appendix, the specific cross section and emissivity are derived for our model.

Tilted Facets

For the quasi-specular component, Fig. A1a shows a schematic illustration of a gently undulating surface that can be divided into sections, or facets. Each facet is large with respect to the wavelength of the Magellan radar (~12.6 cm in a vacuum) and has a radius of curvature that is large with respect to the wavelength. Figure A1b shows the geometry of an individual facet. The frame of reference chosen is planet-centered and right-handed. The vector $\mathbf{z}$ defines the unit normal to the planetary surface and is given by $\mathbf{z} = (0, 0, 1)$. The vector $\mathbf{n}$ defines the unit local normal of the facet and is given by $\mathbf{n} = (\cos \alpha \sin \theta, \sin \alpha \sin \theta, \cos \theta)$, where α is the azimuth of the facet and θ is the inclination of the facet. The vector $\mathbf{e}$ connects the viewer (i.e., Magellan spacecraft antenna) with the facet and defines the emission vector (for calculating emissivity) or the backscatter vector (for calculating specific cross section). It is given by $\mathbf{e} = (-\sin \phi, 0, \cos \phi)$, where ϕ is the emission,

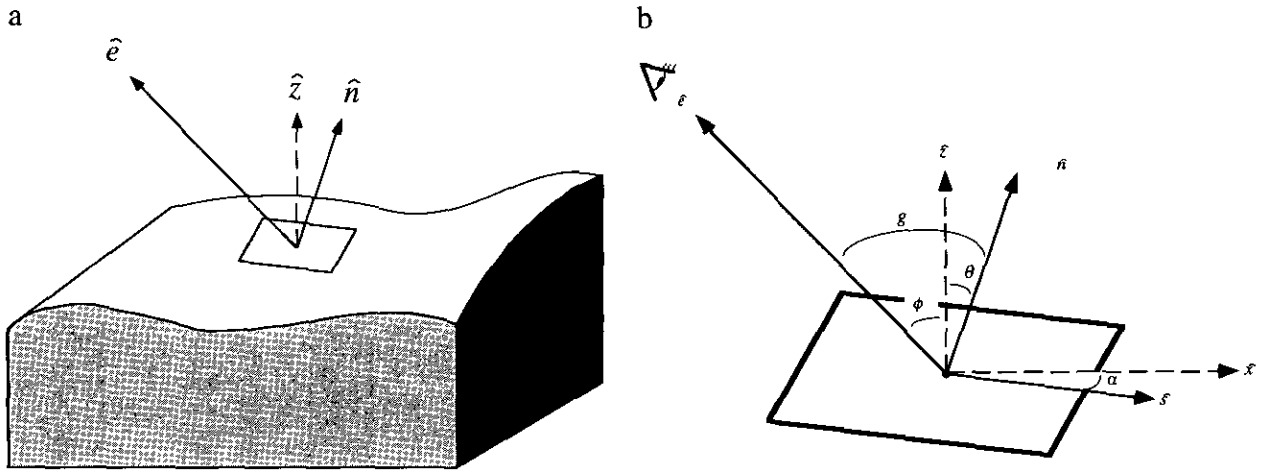

FIG. A1. (a) Schematic illustration of surface modeled using quasi-specular assumption. (b) Illustration of angles and vectors used in scattering model. Parameters are defined in the text.

or equivalently incidence, angle. Note that the **x** axis is defined to lie along the emission vector. The vector **s** defines the unit strike of the facet and is given by $\mathbf{s} = \mathbf{n} \times \mathbf{z}$. Finally, the local emission angle, g, is defined as the angle between the local normal, **n**, and the emission vector, **e**, and is given by $\cos g = \mathbf{n} \cdot \mathbf{e}$.

Having defined the geometry of a single facet, the geometry of a large number of facets is now treated. Previous authors have suggested microwave returns from the Moon and Venus are consistent with distributions of facets governed by Gaussian, exponential, and Hagfors' statistical distributions (Hagfors 1964, Simpson and Tyler 1982, Tyler *et al.* 1992). Various areas of the Moon and Venus are better fit by the various laws than others. For instance, Simpson and Tyler (1982) using data from the Apollo bistatic radar experiment find that exponential and Hagfors' distributions correlate better with lunar maria than highlands. Also, Tyler *et al.* (1992) using the Magellan altimeter find that Hagfors' distribution correlates well with the smoothest portions of Venus whereas Gaussian distributions correlate better with areas that are rough. Because of the well-developed literature concerning microwave scattering from Gaussian surfaces (cf. Ulaby *et al.* 1982) and the goodness-of-fit of the Gaussian distribution to areas of Venus with high RMS slopes, we use the Gaussian distribution.

Consider facet slopes oriented in a Gaussian distribution with respect to inclination, θ, and distributed uniformly with respect to azimuth, α. The number density of facets, $N(\theta)$, can be written

$$N(\theta) = \frac{\sec^3\theta}{\tan^2\sigma_{\mathrm{RMS}}} \exp\left(-\frac{\tan^2\theta}{2\tan^2\sigma_{\mathrm{RMS}}}\right), \tag{A1}$$

where σ_{RMS} is the root-mean-square slope of the surface. Note that Eq. (A1) is not identical to the Gaussian distribution of Tyler *et al.* (1992). The reason for the apparent discrepancy is because their distribution is defined for an adirectional slope distribution whereas we assume an azimuthally uniform slope distribution and present a unidirectional slope distribution.

Specific Cross-Section Model

The specific cross section due to quasi-specular scattering of a undulating surface, $\sigma_{0,QS}$, is the sum of specific cross sections of the facets. A specular ("mirror-like") return only occurs when the local emission angle, g, of a facet is 0°, i.e., when the emission vector and slope normal are coincident. Therefore, the specific cross section of a quasi-specular surface is linearly proportional to the probability density of facets. Following Tyler *et al.* (1992), $\sigma_{0,QS}$ can be written

$$\sigma_{0,QS}(\phi) = \frac{\rho_0}{2\cos\phi} N(\phi), \tag{A2}$$

where ρ_0 is the nadir Fresnel power reflection coefficient which can be calculated using

$$\rho_0 = \left(\frac{\sqrt{\varepsilon} - 1}{\sqrt{\varepsilon} + 1}\right)^2, \tag{A3}$$

where ε is the dielectric constant. In the derivation of the scattering model, we consider only the real portion of the complex dielectric constant. Furthermore, we assume a magnetic permeability of unity. Both of these assumptions are reasonable for most geologic surfaces.

The specific cross section due to diffuse scattering from small-scale texture ($\sigma_{0,D}$) is modeled as dipoles superimposed on the undulating surface (cf. Hagfors and Evans 1968, Pettengill *et al.* 1988, Campbell *et al.* 1993). Following Pettengill *et al.* (1988), $\sigma_{0,D}$ can be written

$$\sigma_{0,D} = 2\rho_0 n \cos^n\phi, \tag{A4}$$

where n is an exponent that controls the decrease of diffuse backscatter with increasing incidence angle. The exponent n is controlled by the spatial distribution of dipole elements; n will be unity for dipoles oriented randomly in three dimensions, whereas n will be 2 for dipoles oriented randomly in only two dimensions (e.g., a flat-lying distribution of dipoles). The ρ_0 term is based upon an implicit assumption that the surface within a footprint is (roughly) homogenous.

The quasi-specular and diffuse components of the specific cross section are combined linearly to determine the observed cross section. Therefore, the observed cross section, σ_0, can be written

$$\sigma_0 = (1 - f_D)\,\sigma_{0,QS} + f_D\sigma_{0,D}$$
$$= (1 - f_D)\frac{\rho_0 \sec^4\phi}{2\tan^2\sigma_{RMS}}\exp\left(-\frac{\tan^2\phi}{2\tan^2\sigma_{RMS}}\right) \quad \text{(A5)}$$
$$+ 2f_D\rho_0 n\cos^n\phi,$$

where f_D is the fraction of backscatter due to diffuse scatter. The justification for the linear addition of the two scattering mechanisms is twofold. The first justification follows from energy conservation: energy not available for scattering due to one mechanism will be available for scattering due to the other mechanism. The second justification is more heuristic and follows from derivations of conventional two-scale theories of scattering that combine Bragg scattering and Kirchoff scattering linearly (cf. Kim and Rodriguez 1992, for detailed discussion of two-scale approaches to radar scattering).

Emissivity Model

We calculate the observed quasi-specular emissivity from our previously defined surface in an analogous fashion to the calculation of specific cross section. Whereas facets with nonzero local emission angles contribute nothing to the observed cross section, facets with nonzero local emission angles will contribute to the observed emissivity. An individual facet will emit energy according to Fresnel's laws. The horizontal and vertical emissivity, e_H and e_V respectively, of a facet with a local emission angle, g, with respect to the Magellan antenna are given by

$$e_H = 1 - \left(\frac{\cos g - \sqrt{\varepsilon - \sin^2 g}}{\cos g + \sqrt{\varepsilon - \sin^2 g}}\right)^2 \quad \text{(A6)}$$

$$e_V = 1 - \left(\frac{\varepsilon\cos g - \sqrt{\varepsilon - \sin^2 g}}{\varepsilon\cos g + \sqrt{\varepsilon - \sin^2 g}}\right)^2. \quad \text{(A7)}$$

The horizontal (H) and vertical (V) emissivity given by Eq. (A6) and (A7) are defined in terms of the frame of reference of the local normal of an individual facet, not in terms of the frame of reference of the Magellan spacecraft antenna. In general, the two frames of references are not coincident. Therefore, the polarized emission received by the antenna will consist of contributions of both horizontal and vertical emission from a local facet. To determine the contributions of the various polarizations to the received emissivity, we define the following vectors. The orientation of the horizontal polarization for the antenna, **h**, is given by **h** = (0, 1, 0). The orientation of the vertical polarization for the antenna, **v**, is given by **v** = (cos ϕ, 0, sin ϕ). Horizontal emission from the facet will occur along the unit vector, **nh**, where **nh** = **n** × **e**. Vertical emission from the facet will occur orthogonally to both the horizontal emission and the emission vector along the unit vector **nv**, where **nv** = **nh** × **n**. Determining the contribution to a given antenna polarization (H or V) from a given facet polarization (H or V) is accomplished by rotating the emission polarization vectors into the frame of reference of the antenna. The fraction of polarization received (X) from a given polarization emitted (Y), f_{XY}, for combinations of H and V polarization can be shown to be

$$f_{HH} = \{[(\mathbf{nh} \times \mathbf{e}) \times \mathbf{e}] \cdot \mathbf{h}\}^2 \quad \text{(A8)}$$

$$f_{HV} = \{[(\mathbf{nv} \times \mathbf{e}) \times \mathbf{e}] \cdot \mathbf{h}\}^2 \quad \text{(A9)}$$

$$f_{VV} = \{[(\mathbf{nv} \times \mathbf{e}) \times \mathbf{e}] \cdot \mathbf{v}\}^2 \quad \text{(A10)}$$

$$f_{VH} = \{[(\mathbf{nh} \times \mathbf{e}) \times \mathbf{e}] \cdot \mathbf{v}\}^2. \quad \text{(A11)}$$

The observed emissivity (in either horizontal or vertical polarization) from a facet due to diffuse scattering will simply be equal to the average of the vertical and horizontal emissivity, or the average of Eq. (A6) and (A7) (Mack and Reiffen 1964, Campbell *et al.* 1993).

The average emissivity of a distribution of facets can now be expressed as the summation of the emissivity of the individual facets weighted by several factors: (1) the probability that a facet has a given inclination, (2) the emissivity of the facet, (3) the projected area of the facet in the direction of emission, (4) the fraction of the observed emissivity of the facet that is horizontally polarized and the fraction that is vertically polarized, and (5) the fraction of the observed emissivity due to quasi-specular versus diffuse scattering. Numerically, this can be written for horizontal and vertical emissivity, respectively, as

$$e_H(\phi) = \frac{\sum_g N(g)\cos g\{(1 - f_D)[e_H(g)f_{HH}(g) + e_V(g)f_{HV}(g)] + (f_D/2)[e_H(g) + e_V(g)]\}}{\sum_g N(g)\cos g} \quad \text{(A12)}$$

$$e_V(\phi) = \frac{\sum_g N(g)\cos g\{(1 - f_D)[e_H(g)f_{VH}(g) + e_V(g)f_{VV}(g)] + (f_D/2)[e_H(g) + e_V(g)]\}}{\sum_g N(g)\cos g} \quad \text{(A13)}$$

There is no simple analytical solution for Eq. (A12) or (A13) and in practice calculation of the emissivity is most easily performed numerically. Note that Eq. (A12) and (A13) have no explicit dependence upon the emission angle, ϕ. In reality, the local emission angle of every facet is dependent upon the emission angle (in addition to the local geometry of the facet). It is possible that a given facet may not be viewable by the Magellan antenna (i.e., it may be "shadowed" by other facets). We investigated shadowing effects (cf. Ulaby *et al.* 1982) and determined that for the range of emission angles viewed by Magellan (≤45°) and the range of roughnesses to be expected on Venus (≤30°?), shadowing effects are negligible. We omit them from this discussion but point out that for some geologic surfaces, shadowing effects are likely to be important.

ACKNOWLEDGMENTS

Support for this research was provided in part by NASA Venus Data Analysis Program Grants NAGW-3419 (REA) and NAGW-3446 (BF), and Planetary Atmospheres Grant NAGW-2867 (BF), Washington University. We thank Gordon Pettengill and Peter Ford for helpful discussions and the generation of ARCDR and GxDR products. We also thank Dr. Pettengill and an anonymous reviewer for detailed comments on an earlier draft of this manuscript and John Wood and Alan Treiman for critical discussions of the geological reality of the ferroelectric model.

REFERENCES

BEVINGTON, P. R. 1969. *Data Reduction and Error Analysis for the Physical Sciences*. McGraw-Hill, New York.

BIENIULIS, M. Z., C. E. CORRY, AND E. R. HOSKINS 1987. Ferroelectricity in natural samples of chalcocite, Cu_2S. *Geophys. Res. Lett.* **14**(2), 135–138.

BRACKETT, R. A., B. FEGLEY, JR., AND R. E. ARVIDSON 1994. Volatile transport on Venus and implications for surface geochemistry and geology. *J. Geophys. Res.*, in press.

BURFOOT, J. C. 1967. *Ferroelectrics: An Introduction to the Physical Principles*. Van Nostrand, London.

CAMPBELL, B. A., R. E. ARVIDSON, AND M. K. SHEPARD 1993. Radar polarization properties of volcanic and playa surfaces: Applications to terrestrial remote sensing and Venus data interpretation. *J. Geophys. Res.* **98**(E9), 17099–17113.

CORRY, C. E. 1984. Ferroelectricity in sulfides and related ore minerals. *EOS Trans. AGU* **65,** 1080–1081.

DEER, W. A., R. A. HOWIE, AND J. ZUSSMAN 1963. *Rock-Forming Minerals,* Vols. 1–5. Wiley, New York.

FEGLEY, B., JR., A. H. TREIMAN, AND V. L. SHARPTON 1993. Venus surface mineralogy: Observational and theoretical constraints. *Proc. Lun. Planet. Sci. Conf. 22nd,* 3–19.

GAVRILOVA, N. D., N. F. KARYAKINA, V. A. KOPTSIK, AND V. K. NOVIK 1970. Segnetoelektricheskiye svoystva minerala stibiotantalita. *Akad. Nauk SSSR* **195**(4), 823–826.

GRIGAS, I., N. N. MOZGOVA, A. ORLYUKAS, AND V. SAMULENIS 1976. The phase transition in $CuSbS_2$ crystals. *Crystallogr. (Sov. Phys.)* **20**(6), 741–742.

HAGFORS, T. 1964. Backscattering from an undulating surface with applications to radar returns from the moon. *J. Geophys. Res.* **69,** 3779–3784.

HAGFORS, T., AND J. V. EVANS 1968. Radar studies of the Moon. In *Radar Astronomy,* McGraw–Hill, New York.

KARGEL, J. S., G. KOMATSU, V. R. BAKER, J. S. LEWIS, AND R. G. STROM 1991. Compositional constraints on outflow channel-forming lavas on Venus. *Lunar Planet. Sci. Conf. 22nd,* 685–686. [Abstract]

KARGEL, J. S., B. FEGLEY, JR., A. H. TREIMAN, AND R. L. KIRK 1994. Carbonate-sulfate volcanism on Venus? *Icarus* **112,** 219–252.

KIM, Y., AND E. RODRIGUEZ 1992. Comparison of the unififed perturbation method with the two-scale expansion. *IEEE Trans. Geosci. Remote Sensing* **30**(3), 510–515.

KINGERY, W. D., H. K. BOWEN, AND D. R. UHLMANN 1976. *Introduction to Ceramics.* Wiley, New York.

KLINGELHÖFER, G., J. FROH, P. HELD, H. JOGER, R. TEUCHER, AND E. KANKELEIT 1992. Development of a Mossbauer backscattering spectrometer, including X-ray fluorescence spectroscopy, for the in situ mineralogical analysis of the Mars surface. In *Workshop on Innovative Instrumentation for the In Situ Study of Atmosphere-Surface Interactions on Mars* (B. Fegley, Jr., and H. Wanke, Eds.), p. 8. LPI Technical Report 92-07, part 1.

KLOSE, K. B., J. A. WOOD, AND A. HASHIMOTO 1992. Mineral equilibria and the high radar reflectivity of Venus mountaintops. *J. Geophys. Res.* **97,** 16,353–16,369.

LEBERL, F. W., J. K. THOMAS, AND K. E. MAURICE 1992. Initial results from the Magellan stereo experiment. *J. Geophys. Res.* **97,** 13,675–13,689.

LINES, M. E. AND A. M. GLASS 1977. *Principles and Applications of Ferroelectrics and Related Materials.* Clarendon Press, Oxford.

MACK, C. L., JR., AND B. REIFFEN 1964. RF characteristics of thin dipoles. *Proc. IEEE* **52,** 533–542.

MOZGOVA, N. N., I. P. GRIGAS, AND A. S. ORLYUKAS 1977. Antimonit; predstavitel' gruppy poluporovdnikovykh segnetoelektrikov. *Zap. Vses. Mineral. Ova.* **6,** 651–658.

PERMENTER, J. L., AND R. L. NUSBAUM 1994. The thick festoon flow and adjacent dark flow, Ovda Regio. *Lunar Planet. Sci. Conf. 25th,* 1067–1068. [Abstract]

PETTENGILL, G. H., P. G. FORD, AND B. D. CHAPMAN 1988. Venus: Surface electromagnetic properties. *J. Geophys. Res.* **93,** 14,881–14,892.

PETTENGILL, G. H., P. G. FORD, AND R. J. WILT 1992. Venus surface radiothermal emission as observed by Magellan. *J. Geophys. Res.* **97,** 13,091–13,102.

RUPPRECHT, G., AND R. O. BELL 1964. Dielectric constant in paraelectric perovskites. *Phys. Rev. Lett.* **135A,** 748–752.

SCHENK, P., AND H. J. MOORE 1992. An unusual thick lava flow in Ovda Regio, Venus. *Lunar Planet. Sci. Conf. 23rd,* 1217–1218.

SEIFF, A. 1983. Appendix A: Models of Venus's atmospheric structure. In Venus (D. M. Hunten, L. Colin, T. M. Donahue, and V. I. Moroz, Eds.), pp. 1045–1048. Univ. of Arizona Press, Tucson.

SENSKE, D. A., R. S. SAUNDERS, AND E. STOFAN 1994. The global geology of Venus: Classification of landforms and geologic history. *Lunar Planet. Sci. Conf. 25th,* 1245–1246. [Abstract]

SHEPARD, M. K., R. E. ARVIDSON, B. FEGLEY, JR., AND R. A. BRACKETT 1994. A ferroelectric model for the low emissivity of highlands on Venus. *Geophys. Res. Lett.* **21**(6), 469–472.

SIMPSON, R. A., AND G. L. TYLER 1982. Radar scattering laws for the lunar surface. *IEEE Trans. Ant. Prop.* **AP-30**(3), 438–449.

SOLOMON, S. C., S. SMREKAR, D. BINDSHADLER, R. GRIMM, W. KAULA, G. MCGILL, R. PHILLIPS, R. SAUNDERS, G. SCHUBERT, S. SQUYRES, AND E. STOFAN 1992. Venus Tectonics: An overview of Magellan observations. *J. Geophys. Res.* **97,** 131,399–13,255.

TRYKA, K. A., AND D. O. MUHLEMAN 1992. Reflection and emission properties on Venus: Alpha Region. *J. Geophys. Res.* **97,** 13,379–13,394.

TYLER, G. L., R. A. SIMPSON, M. J. MAURER, AND E. HOLMANN 1992. Scattering properties of the Venusian surface: Preliminary results from Magellan, *J. Geophys. Res.* **97**(E8), 13,115–13,139.

ULABY, F. T., R. K. MOORE, AND A. K. FUNG 1982. Microwave Remote Sensing: Active and Passive. Addison–Wesley, Reading, MA.

VANIMAN, D. T., D. L. BISH, AND S. J. CHIPERA 1991. In situ planetary surface analyses: The potential of X-ray diffraction with simultaneous X-ray fluorescence. *Lunar Planet. Sci. Conf. 22nd,* 1429–1430.

WILT, R. J. 1992. A study of low radiothermal emissivity on Venus. Ph.D. thesis, MIT.

YESAYAN, S. K., V. V. LEMANOV, G. A. SMOLENSKIY 1974. Otrazheniye i prelomleniye uprugikh voln na domennykh granitsakh v segnetoelektricheskom kristalle $Gd_2(MoO_4)_3$. *Akad. Nauk. SSSR Dokl.* **217**(1), 83–85.

YOUNG, K. F., AND H. P. R. FREDERIKSE 1973. *J. Phys. Chem. Ref. Data* **2,** 313.